A&A, 704, A338 (2025)
https://doi.org/10.1051/0004-6361/202556396

Astronomy & Astrophysics

Parametric strong lensing model of the galaxy cluster Abell 2390 from *Euclid* and MUSE observations

D. Abriola[1,⋆], M. Lombardi[1,3], C. Grillo[1,2], P. Bergamini[1,3], P. Rosati[3,4], M. Meneghetti[3], A. Bolamperti[6,8,7], A. Acebron[9,10,2], G. Granata[5,4,1], G. Angora[4,11,12], H. Atek[13], J. M. Diego[8,9], G. Congedo[14], R. Gavazzi[13,15], Y. Kang[16], M. Montes[17,18], and T. T. Thai[15,19]

(Affiliations can be found after the references)

Received 14 July 2025 / Accepted 12 October 2025

ABSTRACT

We present a new high-precision parametric strong lensing total mass reconstruction of the *Euclid* Early Release Observations (ERO) galaxy cluster Abell 2390 at redshift $z = 0.231$. We include in this analysis 35 multiple images from 13 background sources, of which 25 are spectroscopically confirmed thanks to observations from the Multi Unit Spectroscopic Explorer (MUSE), spanning a redshift range from $z = 0.535$ to $z = 4.877$. After fully re-analysing the MUSE spectroscopy, we combined it with archival spectroscopic catalogues, thus allowing us to select 65 secure cluster members. We further complemented this sample with 114 photometric member galaxies, identified within the *Euclid* VIS and NISP imaging down to magnitude $H_E = 23$. We also measured the stellar velocity dispersions for 22 cluster members in order to calibrate the Faber–Jackson relation and hence the scaling relations for the sub-halo mass components. We tested and compared 11 total mass parametrisations of the galaxy cluster with increasing complexity. To do so, we employed the new parametric strong lensing modelling code `Gravity.jl`. Our best-fit total mass parametrisation is characterised by a single large-scale halo, 179 sub-halo components, and an external shear term. The reference model yields a mean scatter between the model-predicted and observed positions of the multiple images of $0\farcs32$. We were able to quantify the systematics arising from our modelling choices by taking advantage of all the different explored total mass parametrisations. When comparing our results with those from other lensing studies, we noticed an overall agreement in the reconstructed cluster total mass profile in the outermost strong lensing regime. The discrepancy in the innermost region of the cluster (a few kiloparsecs from the brightest cluster galaxy, where few or no strong lensing features are observed) could possibly be ascribed to the different data and modelling choices.

Key words. gravitational lensing: strong – galaxies: clusters: individual: Abell 2390 – galaxies: kinematics and dynamics – cosmology: observations – dark matter

1. Introduction

Strong gravitational lensing (SL) in galaxy clusters is one of the most powerful probes for reconstructing the total mass distribution of their inner dense cores, where multiple images and giant arcs are formed. Once the baryonic mass components have been properly and independently mapped, it is possible to infer the dark matter mass distribution (see, e.g. Bonamigo et al. 2017, 2018; Annunziatella et al. 2017; Mahler et al. 2018; Granata et al. 2022; Meneghetti et al. 2017, 2020, 2022, 2023; Lagattuta et al. 2019; Furtak et al. 2023). Moreover, strong lensing in galaxy clusters can lead to the discovery and study of high-redshift sources (Atek et al. 2023a,b; Roberts-Borsani et al. 2023), the study of the intrinsic properties of background lensed galaxies (Cava et al. 2018; Magaña et al. 2018; Meštrić et al. 2022; Vanzella et al. 2024), and independent probing of the expansion and the geometry of the Universe by means of a variety of techniques, from the use measured time delays between multiple images (Acebron et al. 2023; Bergamini et al. 2024; Grillo et al. 2024) to the use of family ratios (Jullo et al. 2010; Acebron et al. 2017; Caminha et al. 2022; Grillo et al. 2024). To achieve these aims, accurate lensing modelling based on both high-quality imaging and spectroscopy is required, and this need has motivated several SL-dedicated surveys, including the Cluster Lensing And Supernova survey with *Hubble* (CLASH; Postman et al. 2012), the *Hubble* Frontier Fields (HFF; Lotz et al. 2017), and more recently the Beyond Ultra-deep Frontier Fields And Legacy Observations (BUFFALO; Steinhardt et al. 2020) and the Ultradeep NIRSpec and NIRCam ObserVations before the Epoch of Reionization (UNCOVER; Bezanson et al. 2024). The synergy between these projects is aimed at revolutionising the field by helping to develop high-resolution lens models of unprecedented quality.

It is in this context that *Euclid*'s Early Release Observations (ERO; Cuillandre et al. 2025) program Magnifying Lens (Atek et al. 2025) sits. *Euclid* (Euclid Collaboration: Mellier et al. 2025) is an ongoing European Space Agency (ESA) mission aimed at probing cosmology through different methods, ranging from galaxy clustering to weak lensing. In addition to these scopes, *Euclid* is expected to increase the number of SL systems by two orders of magnitude by observing approximately 170 000 galaxy-scale strong lenses (Collett 2015; Acevedo Barroso et al. 2025), roughly 2000 lensed quasars, and thousands of SL features in galaxy clusters distributed in the redshift range $z \in [0.2, 2.0]$ (Euclid Collaboration: Mellier et al. 2025; Boldrin et al. 2012, 2016). These observations will help provide accurate total mass profiles of such systems from the kiloparsec to the megaparsec scale thanks to the ability of the telescope to combine strong and weak lensing measurements in galaxy clusters (Meneghetti et al. 2010, 2014; Merten et al. 2015; Umetsu et al. 2014, 2020) and better understanding the assembly history of these objects. These findings will also further test the predictions of the standard cosmological Lambda cold dark matter (ΛCDM)

⋆ Corresponding author: `davide.abriola@unimi.it`

model and alternative dark matter models. The ERO program Magnifying Lens was developed to target two galaxy clusters, Abell 2390 and Abell 2764. In this paper, we focus on the analysis of the first cluster.

Abell 2390 (hereafter A2390, redshift $z = 0.231$) is one of the richest systems in the Abell galaxy cluster sample (Pello et al. 1991; Le Borgne et al. 1991). It was first selected in a search for arcs on the basis of its bright X-ray emission (Fort 1990; Boehringer et al. 1998; Allen et al. 2001). This system is characterised by elongated arcs (Mellier et al. 1990; Feix et al. 2010; Olmstead et al. 2014; Richard et al. 2021), and it has an estimated mass of $M_{200} \simeq 1.06 \times 10^{15}\,\mathrm{M}_{\odot}$, obtained through a weak lensing analysis (Okabe & Smith 2016)[1]. This cluster was previously subject to several SL studies based on ground and *Hubble* Space Telescope (HST) imaging (Pierre et al. 1996; Pelló et al. 1999; Swinbank et al. 2006) and, thanks to novel *Euclid* observations, to weak lensing analyses as well (Schrabback et al. 2025, Diego et al., in prep.). Thanks to the *Euclid* imaging data from these studies, combined with fully re-analysed archival deep spectroscopy obtained with the Multi Unit Spectroscopic Explorer (MUSE; Bacon et al. 2010, 2014) at the Very Large Telescope (VLT), we are able to develop and present the first high-precision parametric strong lensing model of this cluster based on *Euclid* imaging.

The paper is organized as follows. In Sect. 2 we present the imaging and spectroscopic datasets of A2390 that we used to build our lens models. Section 3 contains the details of the lens models we explored in our work, including the selection of the cluster members and the multiple images, and the total mass parametrisations we studied. The results of the best-fit reference model are then presented and discussed in Sect. 4.

Throughout this paper we use the AB magnitude system and adopt a flat ΛCDM cosmology with $\Omega_{\mathrm{m}} = 0.3$, $\Omega_{\Lambda} = 0.7$, and $H_0 = 70\,\mathrm{km\,s^{-1}\,Mpc^{-1}}$. In this cosmological model, 1″ corresponds to 3.67 kpc at the cluster redshift, $z = 0.231$. The adopted galaxy cluster centre is RA = 328.°403 4183, Dec = 17.°695 474 4 (J2000.0).

2. Data

2.1. Imaging data

The lens cluster A2390 was targeted on 28 November 2023 with both the VISible camera (VIS; Euclid Collaboration: Cropper et al. 2025 and the Near-Infrared Spectrometer and Photometer (NISP; Euclid Collaboration: Jahnke et al. 2025) instruments on board the *Euclid* satellite as part of the performance-verification phase of the mission. Three reference observing sequences (ROS; Euclid Collaboration: Scaramella et al. 2022) were obtained for this galaxy cluster, resulting in three times the nominal *Euclid* Wide Field Survey exposure time. Each ROS had a duration of 70.2 minutes, for a total exposure time of 3.30 hours. The observations were carried out in all of *Euclid*'s four filters (I_{E} on VIS and J_{E}, Y_{E}, and H_{E} on NISP), covering an area of approximately $0.75\,\mathrm{deg}^2$. The resolution of the VIS (NISP) image is 0.″1 (0.″3, respectively), with 5σ point-like sources limiting magnitudes equal to 26.5 for the VIS and 24.5 for the NISP camera. The full data reduction pipeline is described in detail in Cuillandre et al. (2025). A photometric catalogue was extracted from the imaging with the public software `SourceXtractor++` (Kümmel et al. 2022; Bertin et al. 2022). A more in-depth description of the photometric measurements is given in Atek et al. (2025). The astrometric calibration was carried out with the software `SCAMP` (Bertin et al. 2006). The reference catalogue used for the calibration of the ERO data was *Gaia* Data Release 3 (Gaia Collaboration 2023). Figure 1 shows an RGB colour-composite extract of A2390.

We also made use of archival multi-band HST imaging of this cluster (see Sect. 2.2) obtained with the Wide Field and Planetary Camera 2 (WFPC2) within the CYCLE4 HIGH HST Program 5352 (P.I.: Fort, Bezecourt & Soucail 1997). The lens cluster A2390 was observed by HST on 10 December 1994 for a total exposure time of 2100 seconds.

2.2. Spectroscopic data

We made use of archival VLT/MUSE (Bacon et al. 2012) data of A2390, which was observed in the Wide Field Mode for a total integration time of 2 hours in September 2014 within the GTO Program 094.A-0115 (P.I.: Richard, Richard et al. 2021). We employed the datacube available on the ESO Science portal, reduced by the Quality Control Group at the European Southern Observatory (ESO). The reduction process consisted in the removal of instrument signatures, sky subtraction, and combination of the two observing blocks as the latest step. Additionally, we enhanced the background sky subtraction by means of the Zurich Atmosphere Purge (`ZAP`; Soto et al. 2016) tool. The MUSE footprint is shown in red in Fig. 1. The resulting datacube spans the wavelength range from 4750 Å to 9350 Å, with a constant sampling of 1.25 Å/pix; covers a 1′×1′ field of view (FoV); and has a spatial sampling of 0.″2/pix. It has a median point spread function full width half maximum of approximately 0.″83. We registered the astrometry with respect to the HST/F814W image of the cluster.

We built a spectroscopic catalogue of the sources in the MUSE FoV following the procedure adopted in Caminha et al. (2019). We considered a cutout of the HST/F814W image corresponding to the MUSE pointing imprint, and we ran `SExtractor` (`v2.28.0`, Bertin & Arnouts 1996) to detect all the included sources. We used the detected positions as the centres of circular apertures with a radius of 0.″8, within which we extracted a spectrum. This aperture was chosen as to include the majority of the flux of the relative source while reducing the contamination of angularly close-by sources. To this catalogue we also added the sources that do not present a HST/F814W continuum but clear emission lines. These were identified through visual and automatic inspection using the Cube Analysis and Rendering Tool for Astronomy (`CARTA`; Comrie et al. 2021). We extracted their spectra within circular apertures with a radius of 0.″8 centred on the luminosity peak detected in narrow-line images obtained by collapsing the datacube around the wavelengths of the detected lines.

We measured the redshift values for the objects in the catalogue making use of the `Marz` (Hinton et al. 2016) software by identifying spectral features such as emission and absorption lines and continuum breaks through both automatic and visual analyses. We labelled each redshift measurement with a quality flag (QF) defined to be equal to one for tentative measurements, equal to two for possible measurements based on faint spectral features, equal to three for secure measurements based on multiple features, and equal to nine for measurements based on a single emission line. In some cases, if it was possible to characterise the single emission line (e.g. by observing a doublet or the typical asymmetric shape of the Lyα line), we

[1] We note that M_{200} is the total mass enclosed within a sphere with a radius inside which the total mass density of the cluster is 200 times the critical density of the Universe, at the redshift of the cluster.

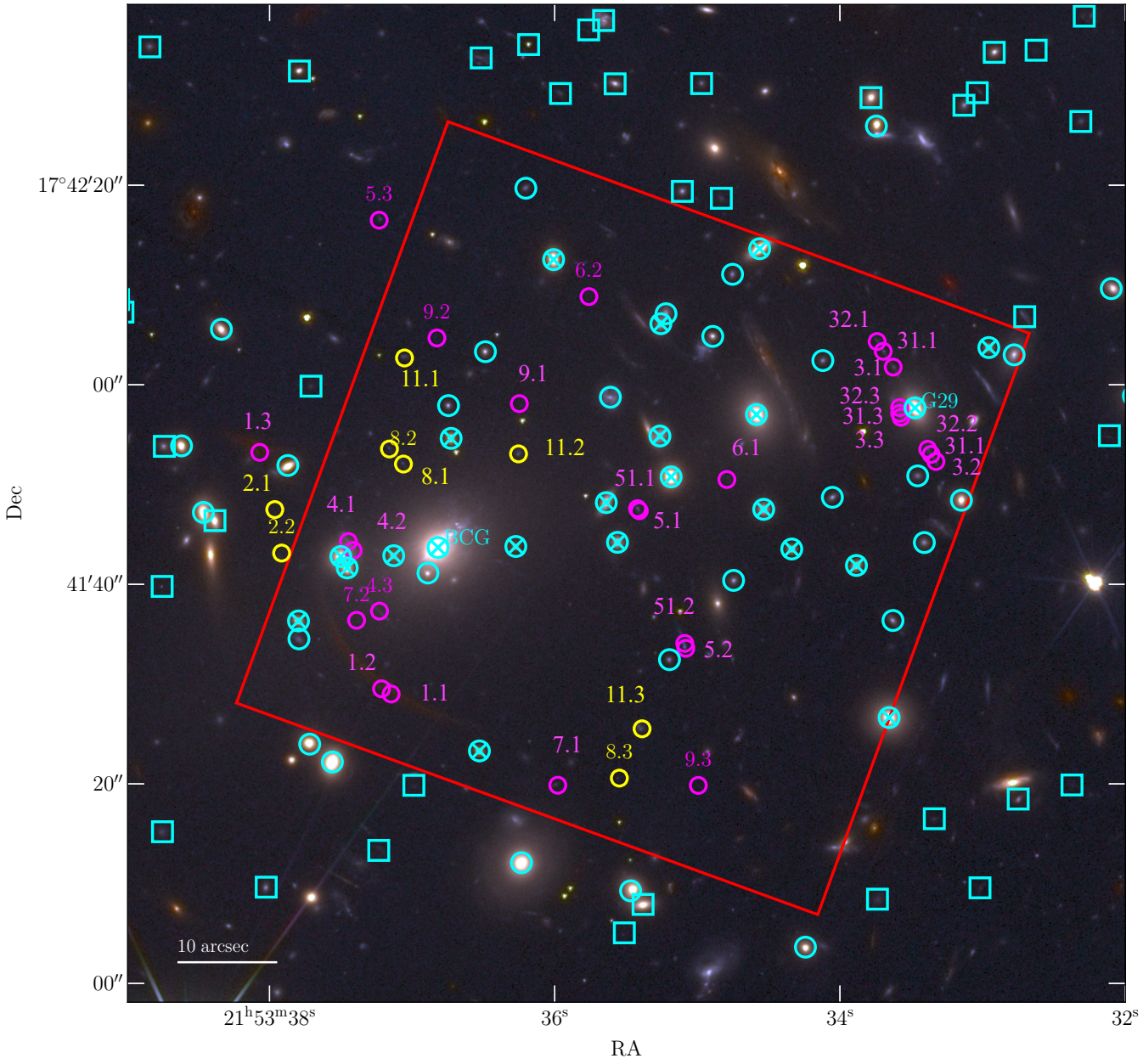

Fig. 1. Colour-composite *Euclid* image (red: H_E, green: $J_E + H_E$, blue: I_E) of the galaxy cluster A2390. The MUSE footprint is shown in red. The spectroscopic (photometric) cluster members are represented with cyan circles (boxes). The 22 cluster members for which we measured the stellar velocity dispersion are further marked with cyan crosses. The spectroscopically confirmed (photometric) multiple images included in our analysis are also shown in magenta (yellow). The multiple images are also labelled with their ID (see Table 1). The positions of the BCG and galaxy G29 (see Sect. 4) are also marked.

converted QF = 9 objects to QF = 3. The final MUSE catalogue contains 96 objects with QF > 2 redshift measurement divided into 6 stars or Galactic objects, 36 cluster members, and 54 background objects, including 25 multiple images from 10 background sources.

Since the MUSE pointing is only restricted to the core of the galaxy cluster (see Fig. 1), we also considered ancillary archival spectroscopic measurements from several catalogues obtained with other instruments in order to complement the MUSE one. Specifically, we used the catalogues by Sohn et al. (2020), based on the SDSS Data Release 14 (Abolfathi et al. 2018) and the 6.5m Multiple Mirror Telescope (MMT) Hectospec spectrograph (Fabricant et al. 2005), and the catalogue by Abraham et al. (1996) based on the Multi Object Spectograph (MOS) and the Subarcsecond Imaging Spectrograph (SIS) at the 3.6m Canada-France-Hawaii Telescope (CFHT). We cross-matched these catalogues in order to produce a final spectroscopic sample. When a source was present in more than one catalogue, we gave priority (if possible) to the redshift measurements obtained through our reduction of the MUSE datacube.

The final full spectroscopic catalogue consists of 592 sources within an effective FoV of approximately $40' \times 20'$. Of these, 36 are foreground galaxies or objects ($z \leq 0.211$), 405 are potential cluster members (i.e. lying in the redshift range $0.211 < z < 0.251$; see Sect. 3.1 for a detailed description of the selection of the cluster members), and 151 are background galaxies

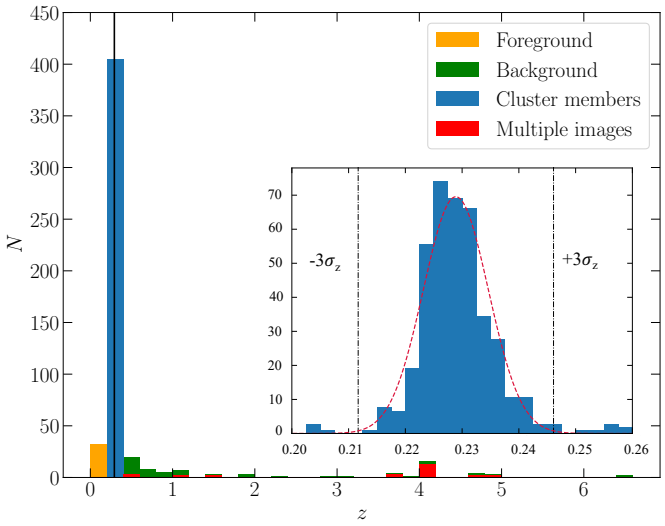

Fig. 2. Spectroscopic redshift distribution of the objects in our final spectroscopic catalogue. Cluster members (i.e. lying in the redshift range from $z = 0.211$ to $z = 0.251$) are in blue, whereas foreground and background objects are in orange and green, respectively. Multiple images are depicted in red. The vertical black line locates the redshift of the galaxy cluster. The insert shows the cluster members selection illustrated in Sect. 3.1. The dashed red line identifies the best-fit Gaussian distribution, whereas the vertical black dotted lines define an interval of $\pm 3\sigma_z$ around the median cluster redshift.

($z \geq 0.251$), including 25 multiple images. Figure 2 displays the redshift distribution of these sources.

3. Strong lensing models

In this section we describe the SL total mass parametrisations of A2390 derived from the imaging and spectroscopic datasets presented in Sect. 2. We performed our analysis with the newly developed software `Gravity.jl` (Lombardi 2024), which allows for the reconstruction of the total mass distribution of a galaxy cluster by means of a Bayesian approach. This approach also enabled us to robustly compare the different mass parametrisations explored. To sample the posterior distribution of the models explored in our work, we employed the non-reversible parallel tempering algorithm (Syed et al. 2019; Surjanovic et al. 2022, 2023) implementation included in `Gravity.jl`. We carried out the optimisations of the lens models in the simplified image-plane configuration. (For further details, see Lombardi (2024).)

In this work, we explored 11 total mass models characterised by the same set of cluster members and multiple images but a different total mass parametrisation. We labelled these total mass models as M1 to M11. A more detailed description of the different mass models is presented in Appendix A. In order to quantify the goodness of our lens models, we adopted two main indicators. First, we estimated the root mean square (RMS) separation between the observed and model-predicted positions of the multiple images. The RMS is defined as

$$\Delta_{\rm RMS} = \sqrt{\frac{1}{N_{\rm im}} \sum_{i=1}^{N_{\rm im}} \left|\boldsymbol{\Delta}_i\right|^2} = \sqrt{\frac{1}{N_{\rm im}} \sum_{i=1}^{N_{\rm im}} \left|\boldsymbol{x}_i^{\rm obs} - \boldsymbol{x}_i^{\rm pred}\right|^2}, \quad (1)$$

where $\boldsymbol{\Delta}_i$ is the difference between the observed ($\boldsymbol{x}_i^{\rm obs}$) and predicted ($\boldsymbol{x}_i^{\rm pred}$) position of the i-th image, and $N_{\rm im}$ is the total number of multiple images considered in the model.

Secondly, we estimated the evidence of the Bayes' theorem. This theorem is used to compute the probability of a set of parameters, $\boldsymbol{p}$, of a model, M, given the observed data, $\boldsymbol{d}$. It can be written as

$$P(\boldsymbol{p}|\boldsymbol{d}, M) = \frac{\mathcal{L}(\boldsymbol{d}|\boldsymbol{p}, M) P(\boldsymbol{p}|M)}{P(\boldsymbol{d}|M)}, \quad (2)$$

where $\mathcal{L}(\boldsymbol{d}|\boldsymbol{p}, M)$ is the likelihood of the data given the parameters, $P(\boldsymbol{p}|M)$ is the prior (i.e. the a priori knowledge of the parameters), and $P(\boldsymbol{p}|\boldsymbol{d}, M)$ is the posterior. The term $P(\boldsymbol{d})$ is a normalisation factor that does not depend on $\boldsymbol{p}$, called evidence. It plays a crucial role in quantifying the goodness of a model in the Bayesian framework. Indeed, the probability, $P(M|\boldsymbol{d})$, that the model, M, is correct when given the data can be estimated by using Bayes's theorem again. Thus we can write

$$P(M|\boldsymbol{d}) = \frac{P(\boldsymbol{d}|M) P(M)}{P(\boldsymbol{d})}. \quad (3)$$

Here, $P(M)$ is a prior over M, that is, our belief that M is the correct model before accessing the data. To compute the normalisation term, $P(\boldsymbol{d})$, one would need to marginalise over all possible models, which is generally impossible. Nevertheless, we can estimate the ratio $P(M|\boldsymbol{d})/P(M'|\boldsymbol{d})$, where M' is an alternative model,

$$\frac{P(M|\boldsymbol{d})}{P(M'|\boldsymbol{d})} = \frac{P(\boldsymbol{d}|M) P(M)}{P(\boldsymbol{d}|M') P(M')}, \quad (4)$$

which quantifies the preference of M over M'. When comparing different modelling choices, we assumed $P(M) = P(M')$. In Table A.1 we quote the RMS and the natural logarithm of the evidence for the different total mass models.

3.1. Cluster members

Cluster members were selected by exploiting both spectroscopic (see Sect. 2.2) and multi-band *Euclid* photometric (Sect. 2.1) information. We first identified a sample of spectroscopically confirmed cluster members starting from our spectroscopic catalogue as follows. We selected those galaxies lying within 1.′5; from the centre of the cluster, which we assumed to be the brightest cluster galaxy (BCG). This choice was motivated by the fact that SL features (i.e. multiple images and giant arcs) are observed within 50 arcseconds from the BCG. The redshift distribution of these galaxies could then be fit with a Gaussian distribution, with mean and standard deviation values of $\hat{z} \pm \sigma_z = 0.231 \pm 0.005$, as depicted in the insert of Fig. 2. We thus identified 65 cluster members (cyan circles in Fig. 1), defined as those lying within $\pm 3\sigma_z$ from $\hat{z}$ (this corresponds to about $\pm 3700\,{\rm km\,s^{-1}}$ around the cluster mean velocity). The magnitude distribution of these galaxies is represented with the orange solid line in Fig. 3.

We completed the spectroscopic sample by adding 114 further photometric (cyan boxes in Fig. 1), bright ($H_{\rm E} < 23$) members by studying the distribution of the galaxies in a colour-magnitude $I_{\rm E} - H_{\rm E}$ versus $H_{\rm E}$ diagram, as shown in Fig. 4. To evaluate the colours, we considered magnitudes measured within a radius of 0.′5 and selected the galaxies lying within 1.′5 from the BCG. We fitted the red cluster sequence (RCS) defined by the above-mentioned 65 spectroscopically confirmed cluster members by means of a weighted linear regression. To do so, we

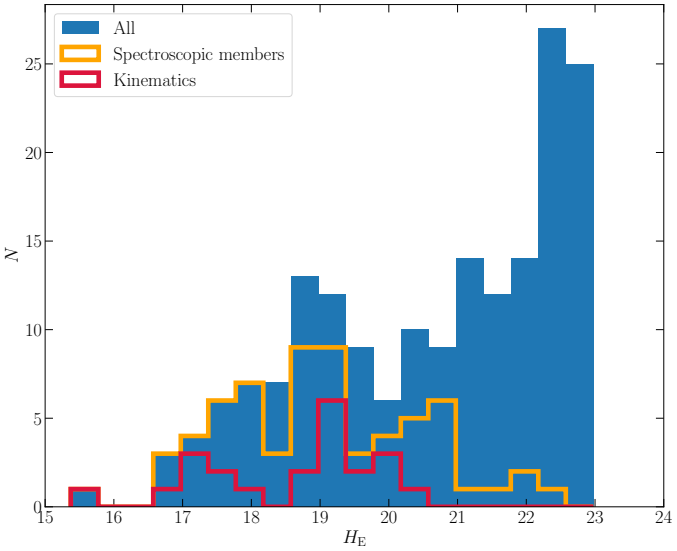

Fig. 3. H_E magnitude distribution of the 179 cluster members included in our models (blue). The 65 spectroscopically confirmed cluster members are highlighted in orange, whereas the sub-sample of the 22 galaxies for which we measured the central stellar velocity dispersion are in red.

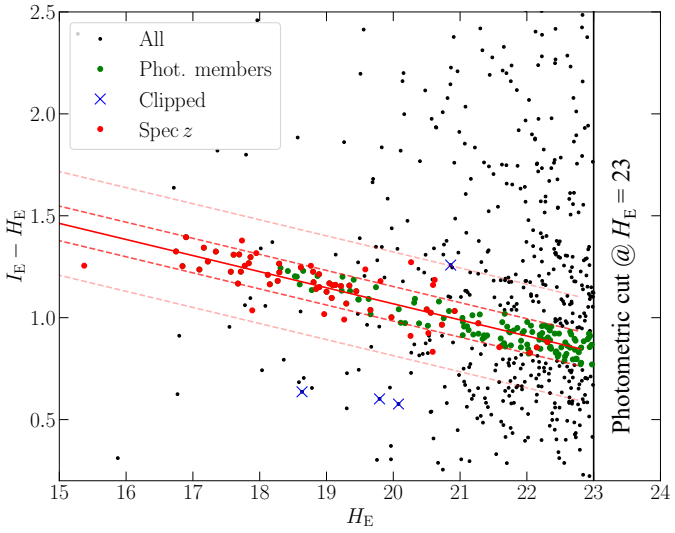

Fig. 4. Colour-magnitude $I_E - H_E$ vs H_E diagram. The red dots represent the 60 spectroscopically confirmed cluster members that we employed to fit the RCS, whereas the four cluster members we discarded due to the clipping are in blue. The green dots are the photometric galaxies added to our cluster member sample. The solid red line is the best-fit RCS, while the dotted ones define a range of $\pm\sigma_{RCS}$ (used for the selection of the cluster members) and $\pm 3\sigma_{RCS}$ (used for the clipping) around the line, respectively.

used the Python package `ltsfit` (Cappellari et al. 2013), which performs a least squares regression by iteratively clipping outliers (Rousseeuw & Van Driessen 2006). The result is presented in Fig. 4. We imposed a 3σ clipping, and thus discarded four members from the fit (represented by the blue crosses in Fig. 4; the red dots are the galaxies we employed for the fit). Given the best-fit, we extended our sample to include galaxies (the green dots in Fig. 4) within $\pm\,\sigma_{RCS} = 0.1$ (the bold red dotted lines) from the RCS best-fit line (the solid red line), with σ_{RCS} as the intrinsic scatter of the data points around the best fit RCS.

Following the procedure presented in Granata et al. (2023, 2025), we measured the line-of-sight stellar velocity dispersion σ_{gal} for several cluster members from the MUSE data (their magnitude distribution is given by the red solid line in Fig. 3). The velocity dispersion measurements were obtained using the spectral fitting code `penalized PiXel-Fitting` (pPXF, Cappellari & Emsellem 2004; Cappellari 2023) to fit the observed spectra to a combination of 463 stellar spectral templates from the X-shooter Spectral Library (XSL) DR2 (Gonneau et al. 2020), convolved with a Gaussian line-of-sight velocity distribution. Following the methods of Cappellari & Emsellem (2004) and Granata et al. (2025), we assessed the statistical uncertainty on the velocity dispersion values by generating 10 000 synthetic MUSE spectra and finding a relation between the statistical error on σ_{gal} and the signal-to-noise ratio $\langle S/N\rangle$. We required a spectral $\langle S/N\rangle$ greater than ten to ensure reliable velocity dispersion measurements, as shown by Bergamini et al. (2019) and Granata et al. (2025). The $\langle S/N\rangle$ threshold required is an average for the whole spectrum, excluding the region masked for the potential influence of sky lines. The average refers to the S/N per spectral bin.

To measure the central stellar velocity dispersion of the cluster galaxies in their central regions, MUSE pixels were weighted by the surface brightness of the members in the *Euclid* VIS band, degraded, and re-binned to match the MUSE point spread function. Spectra were extracted within 1.″5 circular apertures centred on each galaxy, which significantly improved the spectral $\langle S/N\rangle$. Light-weighting the cube resulted in values of the velocity dispersion approximately equivalent to those that would be measured within an aperture corresponding to the effective radius of each galaxy. Our final sample of cluster members with measured stellar velocity dispersion, presented in Table C.1, includes a total of 22 MUSE member galaxies. These are also marked with cyan crosses in Fig. 1. Three of the galaxies for which we measured σ_{gal} showed a spectrum potentially affected by light blending from nearby objects. Hence, for these galaxies we used the unweighted MUSE cube and extracted the spectrum from a fixed 0.″6 aperture in order to reduce the contamination. These objects are marked in Table C.1 with an asterisk. The H_E magnitude distribution of the 179 cluster members included in our models is given in Fig. 3.

3.2. Multiple image systems

Our SL models comprise 35 multiple images from 13 background sources that were identified thanks to *Euclid* and archival HST imaging. Of these, we confirmed 25 (corresponding to ten families) spectroscopically through our reduction of the MUSE datacube, spanning a redshift range between $z = 0.535$ and $z = 4.877$. These are represented with magenta circles in Fig. 1. Systems 1 and 5 are both composed of three multiple images, of which only two had a spectroscopic confirmation. Two families (8 and 11), despite being inside the MUSE footprint, do not show a prominent secure feature that allows us to determine their redshift. An additional family of multiple images (family 2) lies outside the footprint. The redshifts of these three multiple-image systems (families 2, 8, and 11) were then optimized in our lens models with uninformative flat priors between $z = 0.24$ and $z = 10$. These photometric multiple images are shown with yellow circles in Fig. 1. The specifics of the multiple images included in our models are given in Table 1. For each image we report its coordinates, (if possible) its redshift as estimated through the reduction of the MUSE datacube, and the

Table 1. Coordinates and spectroscopic redshifts, with the corresponding MUSE quality flag, of the multiple image systems used to build our models.

ID	$z_{\rm spec}$	QF	RA [deg]	Dec [deg]
1.1	1.038	3	328.404788	17.691397
1.2	1.038	3	328.405068	17.691541
1.3	1.038	–	328.408628	17.698124
2.1	–	–	328.408188	17.696531
2.2	–	–	328.407988	17.695320
3.1	4.048	3	328.390118	17.700497
3.2	4.048	3	328.388868	17.697870
3.3	4.048	3	328.389928	17.699370
31.1	4.048	3	328.390408	17.700937
31.2	4.048	3	328.389008	17.698067
31.3	4.048	3	328.389928	17.699210
32.1	4.048	3	328.390588	17.701209
32.2	4.048	3	328.389108	17.698210
32.3	4.048	3	328.389888	17.699100
5.1	4.048	3	328.397588	17.696557
5.2	4.048	3	328.396178	17.692668
5.3	4.048	–	328.405138	17.704588
51.1	4.048	3	328.397538	17.696498
51.2	4.048	3	328.396208	17.692806
4.1	0.535	3	328.406038	17.695641
4.2	0.535	3	328.405898	17.695396
4.3	0.535	3	328.405235	17.693915
6.1	1.465	3	328.395096	17.697592
6.2	1.465	3	328.399096	17.702482
7.1	4.877	3	328.399918	17.688857
7.2	4.877	3	328.405798	17.693449
8.1	–	–	328.404838	17.698218
8.2	–	–	328.404428	17.697798
8.3	–	–	328.398120	17.689056
9.1	3.653	3	328.401036	17.699392
9.2	3.653	3	328.403273	17.701490
9.3	3.653	3	328.395725	17.688863
11.1	–	–	328.404398	17.700751
11.2	–	–	328.401066	17.698081
11.3	–	–	328.397456	17.690428

Notes. System 2 is outside the MUSE pointing, whereas families 8 and 11 did not display any secure feature, and hence their spectroscopic redshifts and quality flags are not assigned. Images 1.3 and 5.3 do not have spectroscopic confirmation, so we did not assign them a quality flag.

corresponding MUSE quality flag (we follow the same assignment legend introduced previously). In our work, the positions of the multiple images represent the observables for our lens models.

3.3. Total mass parametrisation

The total mass distribution of the galaxy cluster, or, equivalently, the total gravitational potential ϕ of the lens, is parametrised as the sum of three contributions: $N_{\rm h}$ large-scale smooth haloes representing the cluster dark matter component, $N_{\rm g}$ components for the cluster member galaxies, modelled as spherical dual pseudo-isothermal ellipsoid (dPIE) haloes, and a shear-like term which accounts for the presence of massive structures in the outskirts of the system and line-of-sight mass elements. Hence, the total cluster gravitational potential ϕ assumes the form

$$\phi = \sum_{i=1}^{N_{\rm h}} \phi_i^{\rm halo} + \sum_{j=1}^{N_{\rm g}} \phi_j^{\rm gal} + \phi^{\rm shear} . \tag{5}$$

3.4. Dark matter mass distribution

In our work, the large-scale smooth haloes, representing mainly the dark matter component, are modelled as non-singular isothermal ellipsoids (NIEs). This mass distribution is characterised by six free parameters: the position on the sky (x, y); the axis ratio (q), defined as the ratio between the semi-minor and semi-major axes of the projected ellipse; the position angle (θ, computed clockwise from the north axis); the central velocity dispersion (σ); and the core radius, $r_{\rm core}$. The NIE is parametrised in `Gravity.jl` using the following parametrisation (see e.g. Keeton 2001):

$$\Sigma(R') = \frac{\sigma_{\rm v}^2}{2G\sqrt{R'^2 + r_{\rm core}^2}} , \tag{6}$$

with

$$R'^2 = x^2 + y^2/q^2 . \tag{7}$$

In our analyses, we explored the total mass parametrisations including one (models M1–M4 and M9–M10), two (models M5–M8), or three (model M11) dark matter haloes.

3.5. External shear term

The external shear is described in the polar coordinates (r, θ) on the lens plane using the standard parametrisation (see e.g. Keeton 2001) as

$$\phi^{\rm shear}(r, \theta) = \frac{|\gamma|}{2} r^2 \cos[2(\theta - \theta_\gamma)] . \tag{8}$$

Here, $|\gamma|$ is the modulus of the shear and θ_γ is the position angle on the lens plane (also computed clockwise from the north axis), which yields the direction of the shear perturbation.

3.6. Galaxy-scale mass distribution

As mentioned previously, the cluster member galaxies (the sub-halo components of the galaxy cluster) are modelled in terms of spherical dPIE profiles. The spherical dPIE total mass distribution (Limousin et al. 2005; Elíasdóttir et al. 2007; Bergamini et al. 2019) used to model them is described by three free parameters: the central velocity dispersion, σ; the core, $r_{\rm core}$; and the truncation radius, $r_{\rm cut}$. For the i-th cluster member, the central velocity dispersion, $\sigma_{{\rm gal},i}$, and the truncation radius, $r_{{\rm cut},i}$, scale with its luminosity, L_i, according to the following relations (Jorgensen et al. 1996; Natarajan & Kneib 1997; Jullo et al. 2007) – which are introduced to decrease the number of free parameters of the lens model:

$$\sigma_{{\rm gal},i} = \sigma_{\rm ref} \left(\frac{L_i}{L_0} \right)^{\alpha} \tag{9}$$

and

$$r_{{\rm cut},i} = r_{\rm cut,ref} \left(\frac{L_i}{L_0} \right)^{\beta} . \tag{10}$$

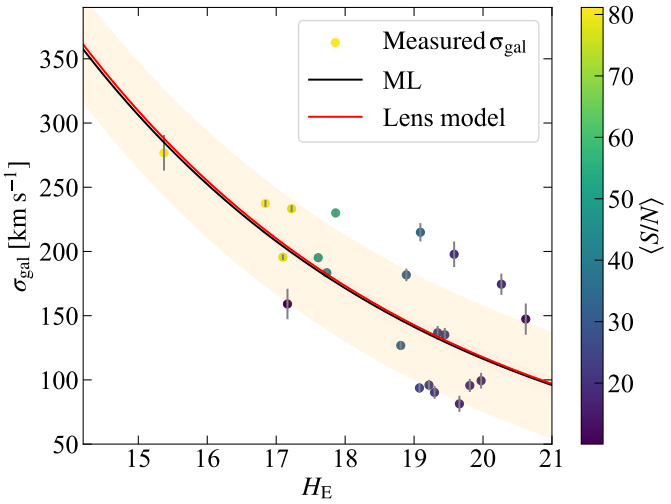

Fig. 5. Measured stellar velocity dispersions of 22 MUSE spectroscopically confirmed cluster members as a function of their *Euclid* H_E magnitudes. Their colours encode the mean signal-to-noise ratio of galaxy spectra. The black solid line is the best-fit (maximum likelihood) of the scaling relation in Eq. (9). The light orange band corresponds to the best-fit mean scatter, $\Delta\sigma_{ap}$, around the best-fit relation. The red solid curve corresponds to the relation in Eq. (9) as obtained with the best-fit parameters of our reference model (see Sect. 3.1). The light red area is estimated from 300 random values of σ_{ref} extracted from the Bayesian MCMC realisations of the reference model of this work.

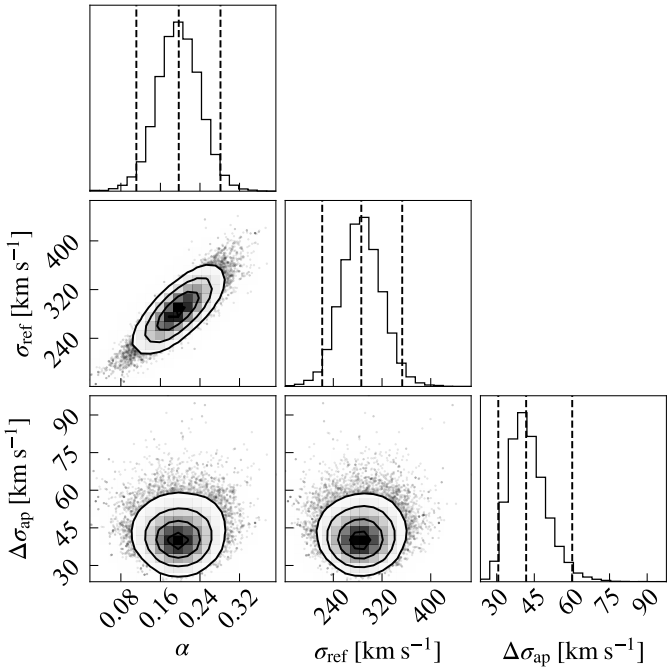

Fig. 6. Posterior probability distribution for the Faber–Jackson relation calibration using the measurements of the velocity dispersion of 22 spectroscopically confirmed cluster members. The 16th, 50th, and 84th percentiles of the marginalised distributions for the slope (α), normalisation (σ_{ref}), and scatter around the scaling relation ($\Delta\sigma_{ap}$) are displayed and shown as vertical dashed lines.

Here, L_0 is a reference luminosity, which we assumed to be that of the BCG. We adopted the total H_E magnitudes in the above scaling relations since they have been proved to be good proxies of the total mass of the galaxies (Grillo et al. 2015; Bergamini et al. 2019). The total magnitude of the BCG in the H_E band is $H_E^{ref} = 15.37$. Following the prescription by Bergamini et al. (2019, 2021), we fitted the values of the slope, α, and the normalisation, σ_{ref}, of Eq. (9), which generalises the Faber–Jackson relation (Faber & Jackson 1976), by employing the measured 22 stellar velocity dispersion velocities, σ_{gal} (see above). We also included an additional free parameter: the intrinsic scatter, $\Delta\sigma_{ap}$, of the measured velocities around the scaling relation. We relied on the Bayesian approach shown in Bergamini et al. (2019) and considered 12 walkers performing 10 000 steps each. We adopted the following uniform priors: $[\alpha_{min}, \alpha_{max}] = [0.0, 1.0]$, $[\sigma_{ref,min}, \sigma_{ref,max}] = [100\,km\,s^{-1}, 600\,km\,s^{-1}]$, and $[\Delta\sigma_{ap,min}, \Delta\sigma_{ap,max}] = [0\,km\,s^{-1}, 100\,km\,s^{-1}]$. The result is shown in Fig. 5. The black solid line is the best-fit scaling relation (obtained with the set of values maximising the likelihood), whereas the light orange band represents the best-fit mean scatter, $\Delta\sigma_{ap}$, around the relation. In Fig. 6, we show the marginalised posterior probability distribution for the Faber–Jackson relation calibration. With respect to previous works by Bergamini et al. (2019, 2021), where the same approach was followed for different lens galaxy clusters, we found a lower median value of α. We recovered $\alpha = 0.21 \pm 0.04$, whereas Bergamini et al. (2019, 2021) found values of $\alpha \in [0.27, 0.30]$.

To determine the value of β, we assumed a fixed scaling relation between the total mass, $M_{tot,i}$, of the i-th cluster member and its luminosity, namely, $M_{tot,i}/L_i \propto L_i^{\gamma}$. Under this assumption, we obtained

$$\beta = \gamma - 2\alpha + 1\,, \tag{11}$$

with $\gamma = 0.2$ in order to be consistent with the observed fundamental plane relation.

Each galaxy is anchored at its measured position (see Tables B.1 and B.2). Moreover, for each sub-halo (galactic) component, the value of the core radius was kept fixed to 0.″005. Given the results of the fit of the generalised Faber–Jackson relation described above, in our models we adopted for σ_{ref} a Gaussian prior with a mean of 285 km s^{-1} and a standard deviation of 41 km s^{-1}, whereas an uninformative prior was assumed on $r_{cut,ref}$. In models M3–M4 and M7–M8, the BCG is excluded from the scaling relations and described independently in terms of a spherical dPIE profile, with both the velocity dispersion and the truncation radius as free parameters. In a similar manner, in models M9 and M10, galaxy G29 (see Fig. 1) is excluded from the scaling relations and modelled either with a spherical (M9) or an elliptical (M10) dPIE mass density profile. This modelling choice was made upon the motivations described in Sect. 4.1.

4. Results and discussion

4.1. Lens models

In Table A.1 we briefly summarise the main properties of the 11 lens models explored in this work, M1 to M11, as well as the principal figures of merit adopted to quantify their goodness. We first explored models comprising one extended or cluster-scale dark matter halo (M1 to M4), and then we added a second halo (models M5 to M8). We also studied the impact of the inclusion (models M2, M4, M6, and M8) or exclusion (models M1, M3, M5, and M7) of an external shear term as well as the removal of the BCG from the scaling relations (models M3, M4, M7, and M8). As shown in Table A.1, the inclusion of an external shear term helps increase the accuracy of the models

Table 2. Input and optimized parameter values of the reference lens model (M9) for the galaxy cluster A2390.

Mass component	Free parameter	Prior	Posterior
Cluster halo	$x_{\rm DM}$ [arcsec]	0 ± 100	2.76 ± 0.08
	$y_{\rm DM}$ [arcsec]	0 ± 100	$1.20^{+0.06}_{-0.05}$
	$q_{\rm DM}$	$0.25 \div 1.0$	0.73 ± 0.01
	$\theta_{\rm DM}$ [rad]	$0 \div \pi$	1.1 ± 0.1
	$\sigma_{\rm DM}$ [km s^{-1}]	$500 \div 1500$	1195 ± 12
	$r_{\rm core,DM}$ [arcsec]	$0.01 \div 30.0$	16.7 ± 0.4
G29	$\sigma_{\rm G29}$ [km s^{-1}]	$50 \div 500$	233^{+5}_{-3}
	$r_{\rm cut,G29}$ [arcsec]	$0.05 \div 25.0$	$18.2^{+4.3}_{-4.1}$
External shear	$\lvert\gamma\rvert$	$0.0 \div 0.3$	0.17 ± 0.01
	θ_γ [rad]	$0 \div \pi$	2.22 ± 0.01
Scaling relations	$\sigma_{\rm ref}$ [km s^{-1}]	285 ± 41	288 ± 5
	$r_{\rm cut,ref}$ [arcsec]	$0.05 \div 30.0$	$16.1^{+1.3}_{-0.9}$

Notes. The first column reports the mass component. The second column contains the parameters of the density profile used to describe the corresponding mass component. The third column shows the prior distributions adopted. When a flat prior on a free parameter value is considered, the boundaries of the prior separated by the ÷ symbol are reported. In case of a Gaussian prior, the notation $a \pm b$ is adopted, with a as the mean and b as the standard deviation of the distribution, respectively. The x and y coordinates are measured with respect to the position of the BCG (RA = 328.°403 408, Dec = 17.°695 475). In the last column, we quote the median value and the 16th and 84th percentiles of the marginalised posterior distribution.

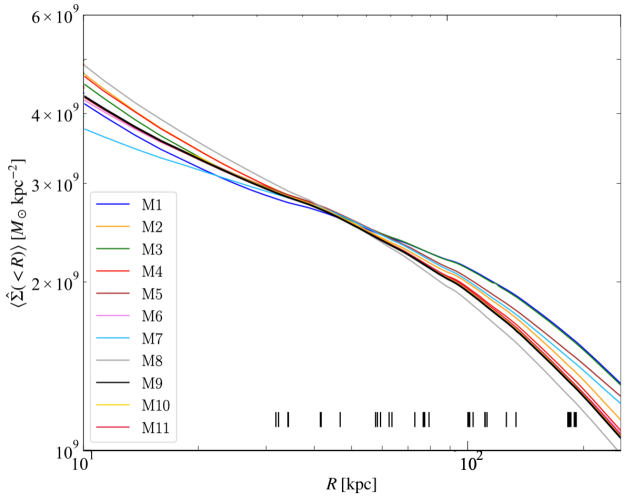

Fig. 7. Average cumulative projected total surface mass density profile of A2390 from the reference (M9, in black) and the other models explored as a function of the projected distance from the BCG. The vertical black lines in the bottom part of the plot are the projected distances from the BCG of the 35 multiple images included in our models.

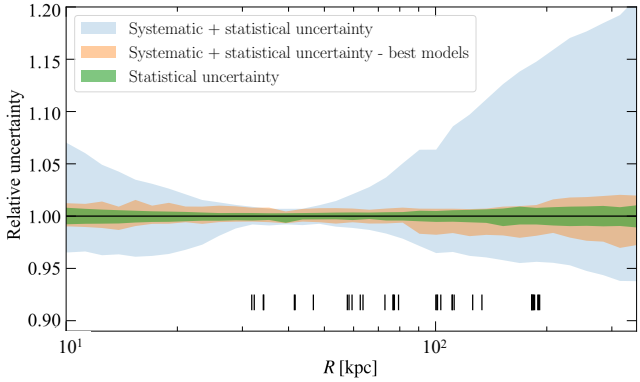

Fig. 8. Relative statistical (green) and total systematic+statistical (blue and orange) uncertainty with respect to the cumulative total mass profile from the reference model. The total error is estimated by considering either all the 11 models explored (in blue) or the three best ones (in orange), according to the figures of merit adopted in this work, namely, M6, M9, and M11.

significantly by reducing the mean scatter between the observed and model-predicted positions of the multiple images by about 0.″1. The exclusion of the BCG from the scaling relations does not seem to critically affect the figures of merit adopted in this work. Despite being the model with the lowest $\Delta_{\rm RMS}$ and highest value of the evidence, M6 predicts the second extended dark matter halo as lying approximately 50″ north-west of the BCG in a region without any concentration of galaxies. Moreover, this second halo is predicted to lie in projection close to galaxy G29 (MUSE ID 29, see Fig. 1 and Table B.1), which is surrounded by the elongated arc where the families 3, 31, and 32 of multiple images are observed. Furthermore, model M6 predicts for the second extended dark matter halo a velocity dispersion value more consistent with that of a cluster member (roughly 300 km s^{-1}). This motivated us to model galaxy G29 independently from the other cluster members by excluding it from the scaling relations. We therefore explored two further models, M9 and M10, where galaxy G29 is described in terms of either a spherical (model M9) or an elliptical (model M10) dPIE mass density profile. We also tested a final model, M11, characterised by three cluster-scale dark matter haloes, which despite the values of RMS and log evidence, can be discarded as well. Indeed, similarly to model M6, the second dark matter halo is predicted to lie in the same region 50″ north-west of the BCG, with a velocity dispersion value consistent with that of a member galaxy. The third one is about 21″ north-west of the BCG, also in a region with no observed cluster members. According to the figures of merit adopted in the paper, M9 stands out as the best-fit model. Hence, in the following, we discuss the results obtained with M9, which is the most physically plausible model and will be considered as the reference model of this work.

The marginalised posterior distributions of the free parameters included in model M9 are given in Fig. A.1. Among the degeneracies observed, we noticed the expected one between the reference velocity dispersion and truncation radius of the scaling relations for the cluster members, namely, $M_{{\rm tot},i} \propto \sigma^2_{{\rm gal},i} r_{{\rm cut},i}$. In addition, we noticed a correlation between the axis-ratio, $q_{\rm DM}$, and the shear, γ: As $q_{\rm DM}$ increases, which implies a rounder cluster-scale halo, the shear increases as well to compensate for the ellipticity. The median value of $\sigma_{\rm ref}$, quoted in Table 2, is consistent with the value recovered by calibrating the Faber-Jackson relation with the kinematics data. In Fig. 5, the red solid curve is the relation obtained by considering the results of M9. We note the difference between the shaded areas: The light orange band represents the intrinsic scatter, $\Delta\sigma_{\rm ap}$, around the relation, whereas the red line was obtained by randomly extracting 300 values of $\sigma_{\rm ref}$ from the Markov chain Monte Carlo (MCMC) realisations for M9. Additionally, the best-fit value of the velocity dispersion of G29 is in very good agreement with our measurement (see Table C.1). Interestingly, the values of the redshifts for families 8 and 11 are consistent with their tentative

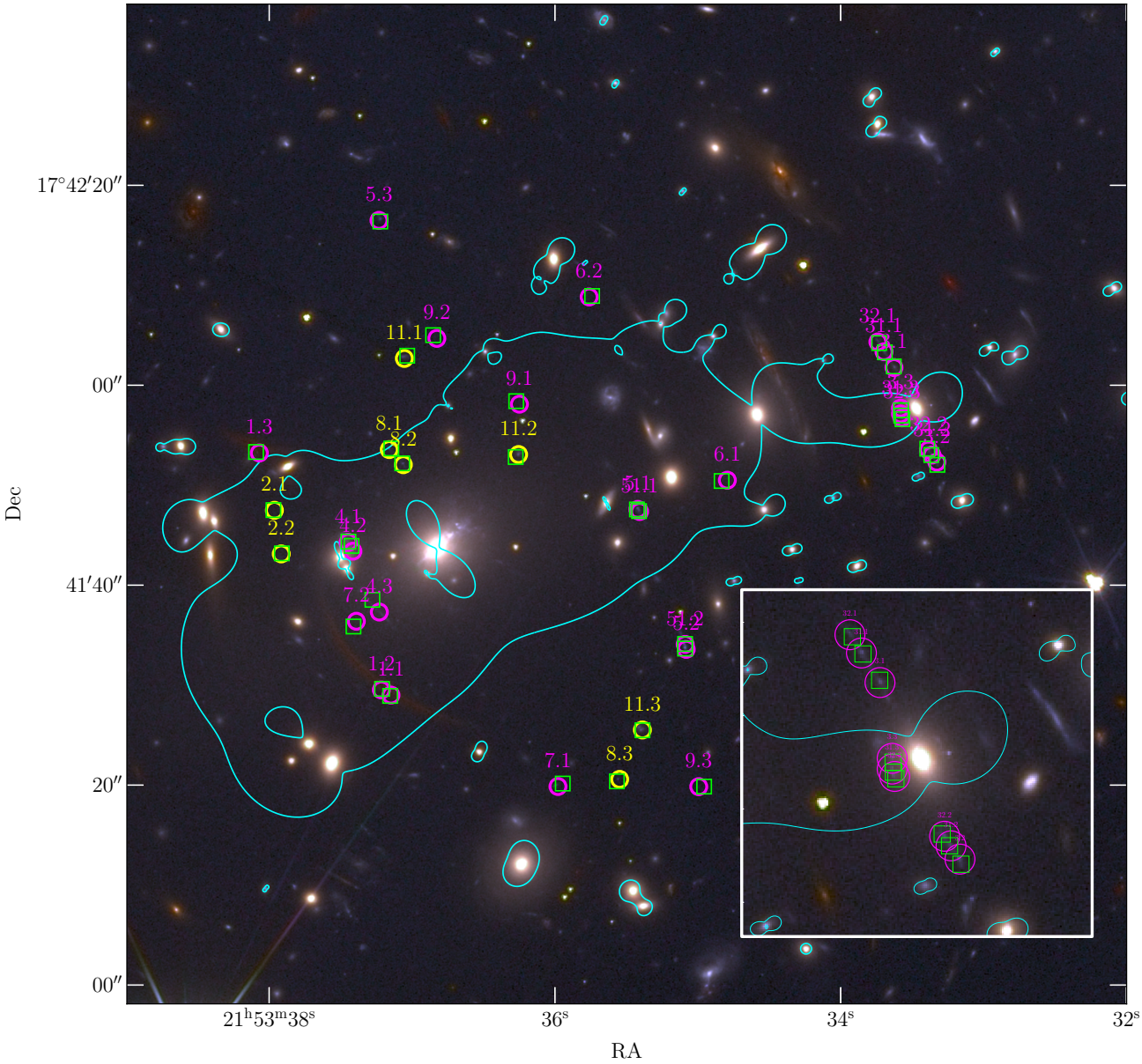

Fig. 9. Colour-composite *Euclid* image (red: H_E, green: J_E + H_E, blue: I_E) of the galaxy cluster A2390 with the critical lines from the reference model M9 evaluated for a source at redshift z_s = 4.048 (families 3, 31, and 32) overlaid in cyan. The spectroscopically confirmed and photometric multiple images included in our analysis are also shown in magenta and yellow, respectively. Green boxes denote the predictions of the reference model. The bottom-right insert depicts a zoom-in of the area around G29.

MUSE spectroscopic measurements. As far the external shear is concerned, its position angle is perpendicular to the direction of the NIE describing the cluster-scale halo.

Model M9 is characterised by a precision of Δ_{RMS} = 0.″32 in reproducing the observed positions of the 35 multiple images used to build the lens models. In Fig. 9, the model-predicted positions of the multiple images are shown as green boxes, and the observed spectroscopically confirmed (photometric) images are displayed as magenta (yellow) circles. Figure 9 also shows the critical curves evaluated at the redshift of families 3, 31, and 32, at z = 4.048, namely, the multiple-image systems lying around G29. The bottom-right insert in the figure shows a zoom-in of the area around G29. A natural extension of the model would be to improve the number of constraints by modelling the surface brightness distribution of the arc where the above-mentioned families are observed.

4.2. Total mass distribution

We find that the cumulative total mass profiles from the 11 parametrisations are in excellent agreement with each other. This is expected since Meneghetti et al. (2017) have showed that the total mass measured within the region where multiple images are observed is the quantity evaluated with better precision. In Fig. 7, for better visualisation, we show the average cumulative projected total surface mass density profiles of the cluster as a function of the distance from the BCG for the reference model of this work (M9) and for the other models explored. As emerges from Fig. 7, the parametrisation of model M9 leads to an isothermal fall-off at large radii. This is expected, as in regions distant from the core of the cluster, no multiple images are observed, and the predictions are thus an extrapolation of the NIE profile adopted. The observed density profile is inconsistent with

the Navarro, Frenk, and White one (Navarro et al. 1996, 1997) expected for cluster haloes (Wang et al. 2020), but this may be attributed to the extrapolation cited above. The predictions of our model are less robust when far from the SL region. We find a projected total mass value of $M(< 40\,\mathrm{kpc}) = (1.40 \pm 0.01) \times 10^{13}\,M_\odot$ within the projected distance of the multiple images from the BCG at which we found the lowest uncertainty (see Fig. 8). The upper and lower limits represent the statistical uncertainty, evaluated as the 84th and 16th percentiles, respectively, estimated by generating 500 total mass profiles from 500 sets of parameters randomly extracted from the MCMC realisations of M9. For model M9, we also estimated the effective Einstein radius, θ_E, as

$$\theta_\mathrm{E} = \sqrt{\frac{A_\mathrm{c}}{\pi}}, \tag{12}$$

with A_c as the area enclosed by the principal critical curve. At redshift $z = 4.048$, we find $\theta_\mathrm{E} = (24.6 \pm 5.4)''$. We randomly extracted 100 points from the MCMC realisations, and for each, we estimated the corresponding θ_E. We quote the median and the uncertainty, evaluated as the semi-difference between the 84th and the 16th quantiles. Thanks to the exploration of the other models, we were able to quantify the systematic uncertainty arising from our modelling choices. For each model, including M9, we generated 500 realisations of the total mass profile, similar to the procedure followed for M9 only. The result, displaying the relative impact of statistical and systematic uncertainties, is shown in Fig. 8, where the blue (green) band corresponds to the interval [16th, 84th] percentiles associated with the total statistical+systematic (statistical only) uncertainty. As is visible in the figure, the uncertainty budget on the cluster total mass is mainly dominated by systematic effects. The total systematic+statistical uncertainty (blue band) can be as large as 15% in the outermost SL region (where the most distant multiple images are observed), with the statistical one (green band) counting up to 0.8%. This systematic uncertainty was estimated by taking into account all the models studied, with no weighing applied according to their RMS or evidence. Nevertheless, if we restrict the sample to the best three models (according to these figures of merit), namely, models M6, M9, and M11, the systematic effects drastically reduce to roughly 1.5% (see the orange band in Fig. 8).

4.3. Comparison with weak lensing

Next, we compared our work with the joint strong and weak lensing analysis first presented in Atek et al. (2025) and then developed in Diego et al. (2025), obtained with the free-form software `WSLAP+` (Diego et al. 2005, 2007) based on the same *Euclid* imaging. Differently from ours, the study relies on a free-form approach and exploits a different set of multiple images to reconstruct the cluster total mass distribution. In Fig. 10, we compare the surface mass density profile obtained in our work (blue curve) with the results from Diego et al. (in prep., orange curve). For a fair comparison, we restricted ourselves to the region where multiple images (represented with vertical black lines) are observed. In the outer regions of the cluster, where no SL features are present, the extrapolation of our reference model indeed becomes less robust. We found a nice agreement in the region between approximately 60 kpc and 500 kpc from the BCG. The discrepancy observed between the two total surface mass density profiles in the innermost (a few tens of kiloparsecs from the BCG) and outermost (a few hundreds of kiloparsecs) regions may be ascribed to the lack of SL features. In particular, in the innermost SL regime, we think that the disagreement can mainly be attributed to the different approach adopted to reconstruct the total mass distribution of the cluster. Meneghetti et al. (2017) have found that parametric models are generally more accurate and precise in reconstructing the projected total mass density of a lens cluster.

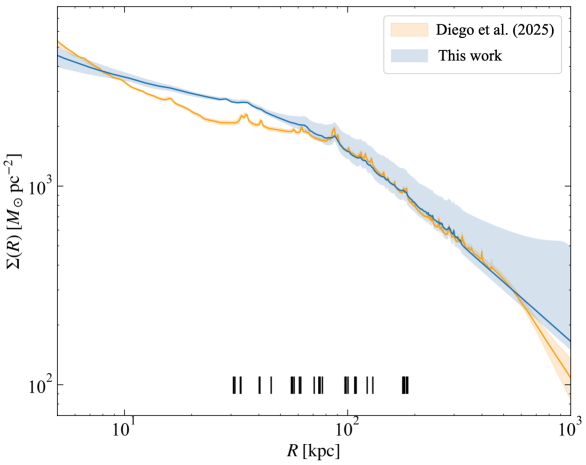

Fig. 10. Surface mass density profile of A2390 as a function of the distance from the BCG. The blue (orange) solid line corresponds to this work (the lens model by Diego et al., in prep.). The light blue area quantifies the systematic uncertainty enclosing the minimum and maximum values of the mass profiles for all 11 models explored in this work. The light orange area is estimated as described in Diego et al. (2025). The vertical black lines in the bottom part of the plot are the projected distances from the BCG of the 35 multiple images included in our models.

5. Conclusions

We have presented new high-precision strong lensing modelling of the *Euclid* ERO galaxy cluster Abell 2390 ($z = 0.231$). To build our model, we combined, for the first time, the Euclid VIS and NISP observations with spectroscopy from MUSE archival data, which we fully re-analysed here. We identified 35 multiple images from 13 background families, 25 of which are spectroscopically confirmed, spanning a redshift range from $z = 0.535$ to $z = 4.877$. We included in our model 65 secure cluster members and added 114 photometric members by studying their distribution in colour and magnitude. We were able to measure the stellar velocity dispersion for 22 cluster members, which allowed us to properly calibrate the sub-halo scaling relations used in the modelling and alleviate inherent degeneracies between the cluster- and the galaxy-scale mass components. We performed our analysis with the new software `Gravity.jl`, with which we explored 11 parametrisations of the total mass distribution of the galaxy cluster with an increasing level of complexity.

The cluster is best described with a single large-scale smooth halo and an external shear term. Our reference model is characterised by a total RMS separation between the observed and model-predicted positions of the 35 multiple images of $\Delta_\mathrm{RMS} = 0\farcs32$. We were able to reconstruct the total mass distribution of the galaxy cluster and estimate the systematic uncertainty arising from our modelling choices by taking advantage of all the models efficiently explored with `Gravity.jl`. On average, full optimisation of a mass model required approximately 2 hours to be obtained on a 64-core workstation, thus allowing us to test different total mass models in a very limited amount of time.

Notably, `Gravity.jl` allows for fast and reliable total mass reconstruction of cluster lenses. Thus, it is an ideal tool for

SL analyses of large samples of galaxy clusters, such as the one that *Euclid* will deliver. Indeed, based on the forecasts by Boldrin et al. (2012, 2016), we expect that *Euclid* will observe SL features in more than 6000 galaxy clusters. These estimates are consistent with the number of SL clusters found in the Q1 data release (Euclid Collaboration: Bergamini et al. 2025). At the same time, `Gravity.jl` will also speed up the analysis of clusters observed at a greater depth compared to *Euclid* observations. As suggested by recent JWST observations, deep follow-up observations of clusters identified in the *Euclid* surveys will likely reveal hundreds of families of multiple images. These observations, combined with spectroscopic follow-up, will enable detailed and robust total mass models with `Gravity.jl`. This study proves that with `Gravity.jl`, robust SL analyses can be achieved in a short amount of time.

Acknowledgements. This work has made use of data from the European Space Agency (ESA) mission Euclid (https://www.cosmos.esa.int/euclid), processed by the Euclid Consortium (https://www.euclid-ec.org/). This work has also made use of the Early Release Observation (ERO) data from the European Space Agency (ESA) mission Euclid, available at https://euclid.esac.esa.int/dr/ero/. This work is based on observations collected at the European Southern Observatory under ESO programme with ID 094.A-0115 (P.I.: Richard). GA acknowledges financial contributions from the agreements of the Euclid ESA mission – ASI/INAF 2018-23-HH.0 Phase D and ASI-INAF n. 2024-10-HH.0 – Phase E. Project partially funded under the National Recovery and Resilience Plan (NRRP), funded by the European Union – NextGenerationEU; Project title "GRAVITY", project code PNRR_BAC24MLOMB_01, CUP C53C22000350006.

References

Abolfathi, B., Aguado, D. S., Aguilar, G., et al. 2018, ApJS, 235, 42
Abraham, R. G., Smecker-Hane, T. A., Hutchings, J. B., et al. 1996, ApJ, 471, 694
Acebron, A., Jullo, E., Limousin, M., et al. 2017, MNRAS, 470, 1809
Acebron, A., Schuldt, S., Grillo, C., et al. 2023, A&A, 680, L9
Acevedo Barroso, J. A., O'Riordan, C. M., Clément, B., et al. 2025, A&A, 697, A14
Allen, S. W., Ettori, S., & Fabian, A. C. 2001, MNRAS, 324, 877
Annunziatella, M., Bonamigo, M., Grillo, C., et al. 2017, ApJ, 851, 81
Atek, H., Chemerynska, I., Wang, B., et al. 2023a, MNRAS, 524, 5486
Atek, H., Shuntov, M., Furtak, L. J., et al. 2023b, MNRAS, 519, 1201
Atek, H., Gavazzi, R., Weaver, J. R., et al. 2025, A&A, 697, A15
Bacon, R., Accardo, M., Adjali, L., et al. 2010, in Ground-based and Airborne Instrumentation for Astronomy III, eds. I. S. McLean, S. K. Ramsay, & H. Takami, SPIE Conf. Ser., 7735, 773508
Bacon, R., Accardo, M., Adjali, L., et al. 2012, The Messenger, 147, 4
Bacon, R., Vernet, J., Borisova, E., et al. 2014, The Messenger, 157, 13
Bergamini, P., Rosati, P., Mercurio, A., et al. 2019, A&A, 631, A130
Bergamini, P., Rosati, P., Vanzella, E., et al. 2021, A&A, 645, A140
Bergamini, P., Schuldt, S., Acebron, A., et al. 2024, A&A, 682, L2
Bertin, E. 2006, in Astronomical Data Analysis Software and Systems XV, eds. C. Gabriel, C. Arviset, D. Ponz, & S. Enrique, ASP Conf. Ser., 351, 112
Bertin, E., & Arnouts, S. 1996, A&AS, 117, 393
Bertin, E., Schefer, M., Apostolakos, N., et al. 2022, Astrophysics Source Code Library [record ascl:2212.018]
Bezanson, R., Labbe, I., Whitaker, K. E., et al. 2024, ApJ, 974, 92
Bezecourt, J., & Soucail, G. 1997, A&A, 317, 661
Boehringer, H., Tanaka, Y., Mushotzky, R. F., et al. 1998, A&A, 334, 789
Boldrin, M., Giocoli, C., Meneghetti, M., et al. 2012, MNRAS, 427, 3134
Boldrin, M., Giocoli, C., Meneghetti, M., et al. 2016, MNRAS, 457, 2738
Bonamigo, M., Grillo, C., Ettori, S., et al. 2017, ApJ, 842, 132
Bonamigo, M., Grillo, C., Ettori, S., et al. 2018, ApJ, 864, 98
Caminha, G. B., Rosati, P., Grillo, C., et al. 2019, A&A, 632, A36
Caminha, G. B., Suyu, S. H., Grillo, C., et al. 2022, A&A, 657, A83
Cappellari, M. 2023, MNRAS, 526, 3273
Cappellari, M., & Emsellem, E. 2004, PASP, 116, 138
Cappellari, M., Scott, N., Alatalo, K., et al. 2013, MNRAS, 432, 1709
Cava, A., Schaerer, D., Richard, J., et al. 2018, Nat. Astron., 2, 76
Collett, T. E. 2015, ApJ, 811, 20
Comrie, A., Wang, K. S., Hsu, S. C., et al. 2021, Astrophysics Source Code Library [record ascl:2103.031]
Cuillandre, J. C., Bertin, E., Bolzonella, M., et al. 2025, A&A, 697, A6
Diego, J. M., Protopapas, P., Sandvik, H. B., et al. 2005, MNRAS, 360, 477
Diego, J. M., Tegmark, M., Protopapas, P., et al. 2007, MNRAS, 375, 958
Diego, J. M., Congedo, G., Gavazzi, R., et al. 2025, A&A, in press, https://doi.org/10.1051/0004-6361/202556372
Elíasdóttir, Á, Limousin, M., Richard, J., et al. 2007, ArXiv e-prints [arXiv:0710.5636]
Euclid Collaboration (Scaramella, R., et al.) 2022, A&A, 662, A112
Euclid Collaboration (Bergamini, P., et al.) 2025, A&A, in press, https://doi.org/10.1051/0004-6361/202554577
Euclid Collaboration (Cropper, M., et al.) 2025, A&A, 697, A2
Euclid Collaboration (Jahnke, K., et al.) 2025, A&A, 697, A3
Euclid Collaboration (Mellier, Y., et al.) 2025, A&A, 697, A1
Faber, S. M., & Jackson, R. E. 1976, ApJ, 204, 668
Fabricant, D., Fata, R., Roll, J., et al. 2005, PASP, 117, 1411
Feix, M., Zhao, H., Fedeli, C., et al. 2010, Phys. Rev. D, 82, 124003
Fort, B. 1990, in Gravitational Lensing, eds. Y. Mellier, B. Fort, & G. Soucail, 360, 219
Furtak, L. J., Zitrin, A., Weaver, J. R., et al. 2023, MNRAS, 523, 4568
Gaia Collaboration (Vallenari, A., et al.) 2023, A&A, 674, A1
Gonneau, A., Lyubenova, M., Lançon, A., et al. 2020, A&A, 634, A133
Granata, G., Mercurio, A., Grillo, C., et al. 2022, A&A, 659, A24
Granata, G., Bergamini, P., Grillo, C., et al. 2023, A&A, 679, A124
Granata, G., Caminha, G. B., Ertl, S., et al. 2025, A&A, 697, A94
Grillo, C., Suyu, S. H., Rosati, P., et al. 2015, ApJ, 800, 38
Grillo, C., Pagano, L., Rosati, P., et al. 2024, A&A, 684, L23
Hinton, S. R., Davis, T. M., Lidman, C., et al. 2016, Astron. Comput., 15, 61
Jorgensen, I., Franx, M., & Kjaergaard, P. 1996, MNRAS, 280, 167
Jullo, E., Kneib, J. P., Limousin, M., et al. 2007, New J. Phys., 9, 447
Jullo, E., Natarajan, P., Kneib, J. P., et al. 2010, Science, 329, 924
Keeton, C. R. 2001, ArXiv e-prints [arXiv:astro-ph/0102341]
Kümmel, M., Álvarez-Ayllón, A., Bertin, E., et al. 2022, ArXiv e-prints [arXiv:2212.02428]
Lagattuta, D. J., Richard, J., Bauer, F. E., et al. 2019, MNRAS, 485, 3738
Le Borgne, J. F., Mathez, G., Mellier, Y., et al. 1991, A&AS, 88, 133
Limousin, M., Kneib, J.-P., & Natarajan, P. 2005, MNRAS, 356, 309
Lombardi, M. 2024, A&A, 690, A346
Lotz, J. M., Koekemoer, A., Coe, D., et al. 2017, ApJ, 837, 97
Magaña, J., Acebrón, A., Motta, V., et al. 2018, ApJ, 865, 122
Mahler, G., Richard, J., Clément, B., et al. 2018, MNRAS, 473, 663
Mellier, Y., Soucail, G., Fort, B., et al. 1990, Gravitational Lensing, 360, 261
Meneghetti, M., Rasia, E., Merten, J., et al. 2010, A&A, 514, A93
Meneghetti, M., Rasia, E., Vega, J., et al. 2014, ApJ, 797, 34
Meneghetti, M., Natarajan, P., Coe, D., et al. 2017, MNRAS, 472, 3177
Meneghetti, M., Davoli, G., Bergamini, P., et al. 2020, Science, 369, 1347
Meneghetti, M., Ragagnin, A., Borgani, S., et al. 2022, A&A, 668, A188
Meneghetti, M., Cui, W., Rasia, E., et al. 2023, A&A, 678, L2
Merten, J., Meneghetti, M., Postman, M., et al. 2015, ApJ, 806, 4
Meštrić, U., Vanzella, E., Zanella, A., et al. 2022, MNRAS, 516, 3532
Natarajan, P., & Kneib, J.-P. 1997, MNRAS, 287, 833
Navarro, J. F., Frenk, C. S., & White, S. D. M. 1996, ApJ, 462, 563
Navarro, J. F., Frenk, C. S., & White, S. D. M. 1997, ApJ, 490, 493
Okabe, N., & Smith, G. P. 2016, MNRAS, 461, 3794
Olmstead, A., Rigby, J. R., Swinbank, M., et al. 2014, AJ, 148, 65
Pelló, R., Kneib, J. P., Le Borgne, J. F., et al. 1999, A&A, 346, 359
Pello, R., Le Borgne, J.-F., Soucail, G., et al. 1991, ApJ, 366, 405
Pierre, M., Le Borgne, J. F., Soucail, G., et al. 1996, A&A, 311, 413
Postman, M., Coe, D., Benítez, N., et al. 2012, ApJS, 199, 25
Richard, J., Claeyssens, A., Lagattuta, D., et al. 2021, A&A, 646, A83
Roberts-Borsani, G., Treu, T., Chen, W., et al. 2023, Nature, 618, 480
Rousseeuw, P. J., & Van Driessen, K. 2006, Data Min Knowl Disc, 12, 29
Schrabback, T., Congedo, G., Gavazzi, R., et al. 2025, Euclid: Early Release Observations. Weak Gravitational Tensing Analysis of Abell 2390
Sohn, J., Fabricant, D. G., Geller, M. J., et al. 2020, ApJ, 902, 17
Soto, K. T., Lilly, S. J., Bacon, R., et al. 2016, MNRAS, 458, 3210
Steinhardt, C. L., Jauzac, M., Acebron, A., et al. 2020, ApJS, 247, 64
Surjanovic, N., Biron-Lattes, M., Tiede, P., et al. 2023, ArXiv e-prints [arXiv:2308.09769]
Surjanovic, N., Syed, S., Bouchard-Côté, A., et al. 2022, ArXiv e-prints [arXiv:2206.00080]
Swinbank, A. M., Bower, R. G., Smith, G. P., et al. 2006, MNRAS, 368, 1631
Syed, S., Bouchard-Côté, A., Deligiannidis, G., et al. 2019, ArXiv e-prints [arXiv:1905.02939]
Umetsu, K., Medezinski, E., Nonino, M., et al. 2014, ApJ, 795, 163
Umetsu, K., Sereno, M., Lieu, M., et al. 2020, ApJ, 890, 148
Vanzella, E., Loiacono, F., Messa, M., et al. 2024, A&A, 691, A251
Wang, J., Bose, S., Frenk, C. S., et al. 2020, Nature, 585, 39

[1] Dipartimento di Fisica, Università degli Studi di Milano, Via Celoria 16, I-20133 Milano, Italy
[2] INAF-IASF Milano, Via A. Corti 12, I-20133 Milano, Italy
[3] INAF-OAS, Osservatorio di Astrofisica e Scienza dello Spazio di Bologna, Via Gobetti 93/3, I-40129 Bologna, Italy
[4] Dipartimento di Fisica e Scienze della Terra, Università degli Studi di Ferrara, Via Saragat 1, I-44122 Ferrara, Italy
[5] Institute of Cosmology and Gravitation, University of Portsmouth, Burnaby Rd, Portsmouth PO1 3FX, UK
[6] Dipartimento di Fisica e Astronomia, Universitá degli Studi di Padova, Vicolo dell'Osservatorio 3, I-35122 Padova, Italy
[7] INAF-Osservatorio Astronomico di Padova, Vicolo dell'Osservatorio 5, I-35122 Padova, Italy
[8] European Southern Observatory, Karl-Schwarzschild-Str. 2, D-85748 Garching bei München, Germany
[9] Instituto de Fisica de Cantabria (IFCA), CSIC – Universidad de Cantabria, Avda. losAvda. los Castros, s/n, E-39005 Santander, Spain
[10] Departamento de Fisica Moderna, Universidad de Cantabria, Avda. de los Castros s/n, E-39005 Santander, Spain
[11] INAF–Osservatorio Astronomico di Capodimonte, Via Moiariello 16, I-80131 Napoli, Italy
[12] INAF-OAT Osservatorio Astronomico di Trieste, Via G. B. Tiepolo 11, I-34131 Trieste, Italy
[13] Institut d'Astrophysique de Paris, UMR 7095, CNRS, and Sorbonne Université, 98 bis boulevard Arago, 75014 Paris, France
[14] Institute for Astronomy, University of Edinburgh, Royal Observatory, Blackford Hill, Edinburgh EH9 3HJ, UK
[15] Aix-Marseille Université, CNRS, CNES, LAM, Marseille, France
[16] Department of Astronomy, University of Geneva, ch. d'Ecogia 16, 1290 Versoix, Switzerland
[17] Instituto de Astrofísica de Canarias, Calle Vía Láctea s/n, 38204 San Cristóbal de La Laguna, Tenerife, Spain
[18] Departamento de Astrofísica, Universidad de La Laguna, 38206 La Laguna, Tenerife, Spain
[19] National Astronomical Observatory of Japan, 2-21-1 Osawa, Mitaka Tokyo 181-8588, Japan

Appendix A: Total mass parametrisations

In Table A.1 we present a brief summary of the lens models explored in this work, M1 to M11. For each of them, a brief description of the parametrisation is given, as well as the number of free parameters, the degrees of freedom, and the two figures of merit used to quantify their goodness adopted in our analysis, the RMS $\Delta_{\rm RMS}$ and the evidence of Bayes' theorem.

Table A.1. Description of the lens models explored in this work.

Model	$N_{\rm par}$	$N_{\rm dof}$	$\Delta_{\rm RMS}$ [″]	$-\ln E$	Description
M1	11	33	0.52	592	One cluster-scale DM halo, 179 sub-halo components
M2	13	31	0.40	476	One cluster-scale DM halo, 179 sub-halo components, an external shear-like term
M3	13	31	0.53	651	One cluster-scale DM halo, 179 sub-halo components, with the BCG excluded from the scaling relations
M4	15	29	0.39	479	One cluster-scale DM halo, 179 sub-halo components, with the BCG excluded from the scaling relations, an external shear-like term
M5	17	27	0.41	445	Two cluster-scale DM haloes, 179 sub-halo components
M6	19	25	0.31	379	Two cluster-scale DM haloes, 179 sub-halo components, an external shear-like term
M7	19	25	0.41	461	Two cluster-scale DM haloes, 179 sub-halo components, with the BCG excluded from the scaling relations
M8	21	23	0.34	393	Two cluster-scale DM haloes, 179 sub-halo components, with the BCG excluded from the scaling relations, an external shear-like term
M9	15	29	0.32	397	One cluster-scale DM halo, 179 sub-halo components, an external shear-like term, with galaxy G29 excluded from the scaling relations (spherical dPIE density profile)
M10	17	27	0.32	399	One cluster-scale DM halo, 179 sub-halo components, an external shear-like term, with galaxy G29 excluded from the scaling relations (elliptical dPIE density profile)
M11	19	25	0.27	363	Three cluster-scale DM haloes, 179 sub-halo components, an external shear-like term

Notes. $N_{\rm par}$ and $N_{\rm dof}$ are the number of model free-parameters and the degrees-of-freedom, respectively. $\Delta_{\rm RMS}$ is the RMS displacement between the positions of observed and model-predicted multiple images. $\ln E$ is the natural logarithm of the evidence of Bayes' theorem for each model. In the last column, we briefly summarise the total mass parametrisation of the lens model.

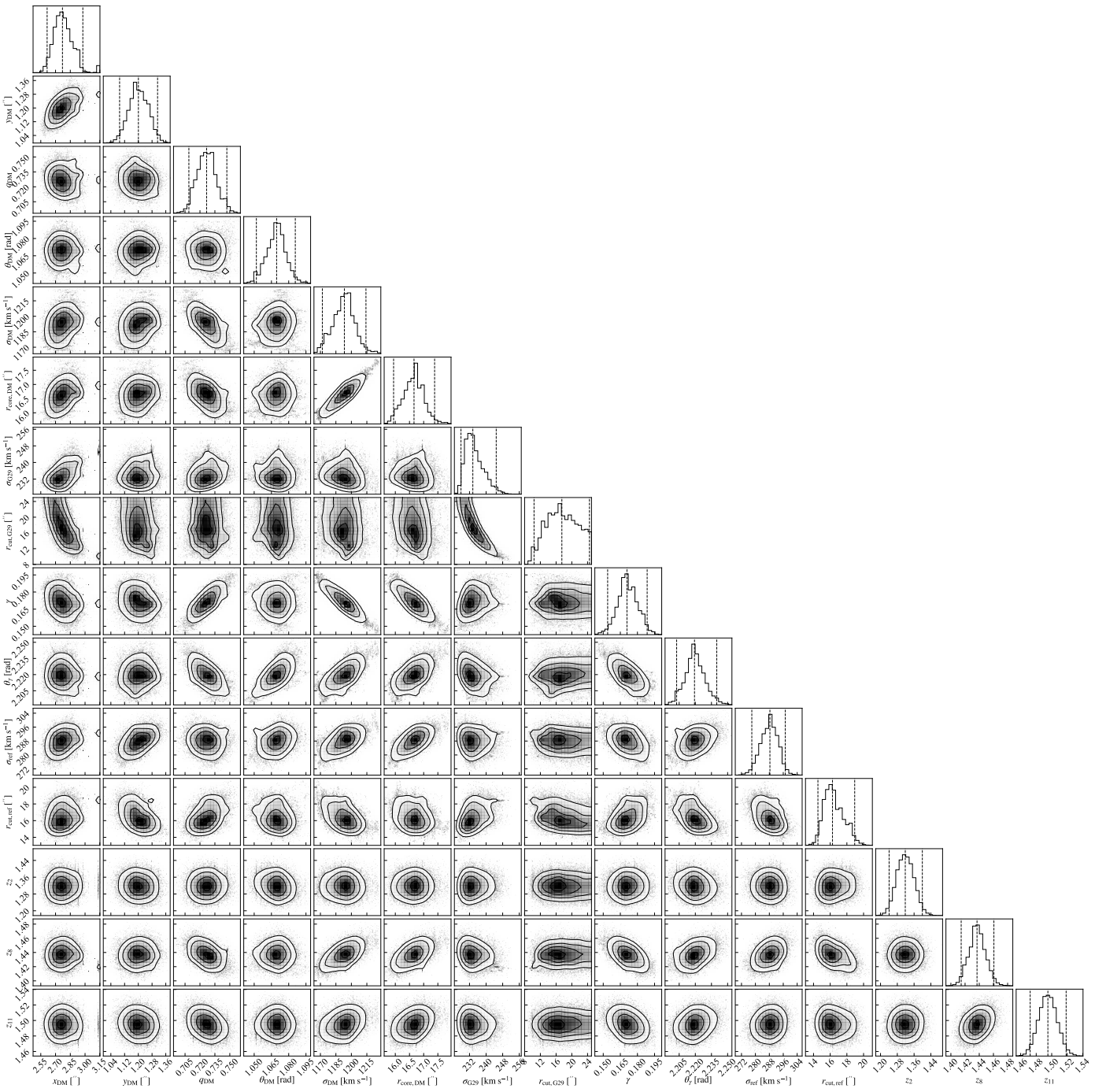

Fig. A.1. Marginalised posterior distributions of the parameters of the reference model of this work, M9. The 16th, 50th and 84th percentiles of the marginalised distributions are shown as vertical dashed lines.

Appendix B: Cluster members catalogue

In this Appendix, we present the catalogue of the cluster members included in our total mass parametrisations. Table B.1 lists the 65 spectroscopically confirmed cluster members, identified by their ID, position, spectroscopic redshift, and H_E magnitude. Table B.2 lists the 114 photometric cluster members, for which we report their position and H_E magnitude.

Table B.1. ID, coordinates, spectroscopic redshift, and H_E magnitude of the spectroscopic cluster members included in the models explored in this work.

ID	RA [deg]	Dec [deg]	z_{spec}	H_E
1	328.403418	17.695474	0.2301	15.37
129	328.400980	17.686700	0.2465	16.75
29	328.389480	17.699362	0.2243	16.84
132	328.406506	17.689503	0.2294	16.90
23	328.394113	17.699178	0.2301	17.10
6	328.390237	17.690741	0.2284	17.16
13	328.396608	17.697441	0.2317	17.22
135	328.380951	17.692656	0.2459	17.34
139	328.428199	17.698142	0.2238	17.57
65	328.394020	17.703793	0.2263	17.61
123	328.419564	17.680547	0.2313	17.67
117	328.403859	17.676102	0.2275	17.69
145	328.424179	17.704111	0.2433	17.72
5	328.406259	17.695223	0.2280	17.73
138	328.410274	17.696451	0.2311	17.78
128	328.397792	17.685917	0.2278	17.84
58	328.400041	17.703490	0.2317	17.86
118	328.416810	17.676787	0.2404	17.89
134	328.407167	17.690000	0.2335	17.95
555	328.426530	17.690097	0.2263	18.12
144	328.420311	17.703075	0.2226	18.15
142	328.383097	17.699696	0.2372	18.27
456	328.407807	17.697758	0.2346	18.29
116	328.414478	17.673639	0.2353	18.29
140	328.410913	17.698304	0.2290	18.62
121	328.422178	17.679424	0.2155	18.63
549	328.390609	17.707208	0.2320	18.77
37	328.388124	17.696791	0.2255	18.80
33	328.398502	17.696725	0.2346	18.81
481	328.391098	17.714808	0.2321	18.84
21	328.406071	17.694906	0.2275	18.89
143	328.409748	17.701550	0.2275	18.89
54	328.386584	17.700838	0.2348	18.97
454	328.401332	17.673742	0.2391	19.00
452	328.383745	17.702682	0.2319	19.04
34	328.393902	17.696538	0.2278	19.08
48	328.403036	17.698513	0.2260	19.09
126	328.392682	17.684349	0.2312	19.13
22	328.398174	17.695619	0.2316	19.22
501	328.415601	17.707220	0.2339	19.27
41	328.396935	17.698578	0.2201	19.30
27	328.391192	17.694975	0.2299	19.34
15	328.407495	17.693431	0.2422	19.45
8	328.402209	17.689812	0.2262	19.58
59	328.396907	17.701705	0.2411	19.66
14	328.407482	17.692931	0.2446	19.79
32	328.393082	17.695434	0.2268	19.81
61	328.387322	17.701042	0.2246	19.97
49	328.398382	17.699659	0.2284	20.08
46	328.389401	17.697469	0.2418	20.26
28	328.404712	17.695246	0.2313	20.27
63	328.392174	17.700680	0.2303	20.50
25	328.394782	17.694560	0.2294	20.52
62	328.402033	17.700927	0.2235	20.56
39	328.391895	17.696872	0.2208	20.59
64	328.395390	17.701352	0.2319	20.60
35	328.401145	17.695504	0.2318	20.62
66	328.396756	17.701983	0.2241	20.73
18	328.403713	17.694764	0.2306	20.86
31	328.389208	17.695613	0.2334	20.92
17	328.390124	17.693444	0.2404	21.27
57	328.403111	17.699426	0.2257	21.59
12	328.396655	17.692354	0.2373	22.05
69	328.394812	17.703081	0.2324	22.15
75	328.400852	17.705477	0.2375	22.31

Table B.2. Coordinates and H_E magnitude of the photometric cluster members included in the models explored in this work.

RA [deg]	Dec [deg]	H_E
328.395373	17.679027	18.31
328.419201	17.684186	18.42
328.409937	17.696223	18.53
328.397427	17.685539	18.56
328.422078	17.691723	18.60
328.425706	17.690011	18.65
328.379492	17.690138	18.78
328.390766	17.707999	18.87
328.388423	17.712424	19.23
328.387095	17.712811	19.24
328.419327	17.708467	19.35
328.420524	17.707458	19.41
328.390916	17.679384	19.48
328.398056	17.673459	19.48
328.417843	17.679514	19.63
328.423359	17.708350	19.66
328.383745	17.681237	19.74
328.421229	17.679324	20.08
328.398580	17.710146	20.11
328.407470	17.708739	20.18
328.387165	17.709260	20.31
328.388858	17.680391	20.32
328.411416	17.698291	20.39
328.398244	17.708383	20.52
328.386466	17.688472	20.68
328.397987	17.700801	20.75
328.414557	17.690027	20.83
328.392893	17.694584	21.04
328.388050	17.707786	21.04
328.395030	17.692832	21.04
328.398450	17.697732	21.06
328.378788	17.694668	21.10
328.387660	17.708136	21.13
328.406028	17.678437	21.18
328.396279	17.705389	21.20
328.395716	17.708390	21.27
328.400771	17.709475	21.30
328.412377	17.674895	21.34
328.395140	17.705197	21.36
328.421231	17.697061	21.37
328.405221	17.712687	21.40
328.400367	17.702921	21.61
328.405150	17.687042	21.62
328.412625	17.702028	21.63
328.408438	17.686019	21.66
328.425366	17.696199	21.67
328.412807	17.711701	21.68
328.411456	17.676374	21.71
328.384534	17.710268	21.73
328.393620	17.718180	21.75
328.397974	17.684747	21.76
328.418133	17.683454	21.80
328.411837	17.709412	21.86
328.417213	17.706249	21.91
328.384429	17.681682	21.91
328.416339	17.683650	21.93
328.379613	17.692168	21.96
328.412754	17.702376	22.01
328.387582	17.686001	22.01
328.383801	17.698588	22.02
328.417443	17.690444	22.03
328.400688	17.674176	22.06
328.401678	17.679097	22.08
328.397523	17.690469	22.19
328.414195	17.689926	22.19
328.420850	17.681010	22.20
328.390874	17.702680	22.20
328.426985	17.698382	22.23
328.392301	17.678618	22.23
328.390167	17.692743	22.25
328.417624	17.675773	22.28
328.404124	17.688855	22.31
328.386274	17.701900	22.31
328.390865	17.682477	22.33
328.395132	17.679975	22.34
328.390577	17.685685	22.34
328.394710	17.674228	22.35
328.382411	17.703971	22.35
328.402158	17.709105	22.36
328.414735	17.697317	22.37
328.404436	17.697823	22.42
328.399016	17.709886	22.43
328.417525	17.695840	22.44
328.399131	17.703406	22.46
328.411468	17.687562	22.48
328.400644	17.677260	22.48
328.394823	17.692407	22.52
328.422040	17.686636	22.56
328.399841	17.708115	22.57
328.379403	17.692802	22.57
328.424205	17.703253	22.59
328.382970	17.698536	22.61
328.384634	17.707335	22.65
328.415015	17.687250	22.65
328.392229	17.681096	22.66
328.400346	17.708374	22.69
328.398442	17.704258	22.71
328.380145	17.703602	22.72
328.391982	17.717290	22.73
328.418263	17.684292	22.74
328.415171	17.696093	22.75
328.392433	17.693603	22.78
328.424831	17.701809	22.80
328.400695	17.678667	22.81
328.407131	17.699966	22.81
328.388916	17.687924	22.81
328.381149	17.693650	22.85
328.388185	17.715269	22.91
328.398344	17.685101	22.93
328.388076	17.678557	22.93
328.382448	17.707600	22.94
328.411479	17.694391	22.95
328.385941	17.709318	22.97
328.384893	17.688864	22.97

Appendix C: Measured velocity dispersion catalogue

In this Appendix, we present the final MUSE velocity dispersion catalogue, containing velocity dispersion measurements for 22 cluster members, as discussed in Sect. 3.1.

Table C.1. Catalogue of measured velocity dispersion values.

ID	RA [deg]	Dec [deg]	z_{spec}	σ_{gal} [km s^{-1}]	$\delta\sigma_{gal}$ [km s^{-1}]	$\langle S/N \rangle$
1	328.403418	17.695474	0.2301	276.8	13.8	81.1
3	328.395241	17.693922	0.5212	114.1	4.4	28.0
5*	328.406259	17.695223	0.2280	183.4	3.6	45.2
8	328.402209	17.689812	0.2262	197.8	10.0	19.2
13	328.396608	17.697441	0.2317	233.3	2.6	77.7
15	328.407495	17.693431	0.2422	135.2	5.3	24.3
21*	328.406071	17.694906	0.2275	181.7	4.9	32.6
22	328.398174	17.695619	0.2316	96.0	4.0	23.0
23	328.394113	17.699178	0.2301	195.5	2.2	77.5
27	328.391192	17.694975	0.2299	136.7	5.3	24.0
28*	328.404712	17.695246	0.2313	174.5	8.3	18.8
29	328.389480	17.699362	0.2243	237.3	2.7	81.0
32	328.393082	17.695434	0.2268	95.7	5.1	17.6
33	328.398502	17.696725	0.2346	126.8	3.4	32.7
34	328.393902	17.696538	0.2278	93.7	3.9	24.4
35	328.401145	17.695504	0.2318	147.4	12.2	12.7
41	328.396935	17.698578	0.2201	90.3	5.0	21.8
48	328.403036	17.698513	0.2260	215.0	7.1	33.3
58	328.400041	17.703490	0.2317	230.0	3.4	56.3
59	328.396907	17.701705	0.2411	81.4	6.3	18.6
61	328.387322	17.701042	0.2246	99.4	6.1	17.2
65	328.394020	17.703793	0.2263	195.1	3.2	49.5
136	328.390237	17.690741	0.2279	159.1	11.9	10.1

Notes. We identify the galaxies included in this catalogue with their ID. We report the spectroscopic redshift of the galaxy z_{spec} (fourth column), its measured velocity dispersion value with σ_{gal} (fifth column), its uncertainty with $\delta\sigma_{gal}$ (sixth column), and the spectral $\langle S/N \rangle$ (seventh column). We mark the members potentially affected by light blending, for which we used a smaller aperture (0.6″ in radius, see Sect. 3.1) for the spectral extraction, with *.